Boron-doped diamond decorated with metal-organic framework-derived compounds for high-voltage aqueous asymmetric supercapacitors

Liao, Shuling; Peng, Chong; Zou, Jifeng; Mandal, Soumen; WILLIAMS, Oliver; Huang, Xinyi; Zhao , Mingwei; Xu, Jing; Yu, Siyu & YANG, Nianjun (2024)
Boron-doped diamond decorated with metal-organic framework-derived compounds for high-voltage aqueous asymmetric supercapacitors. In: Carbon, 230 (Art N° 119651).

DOI: 10.1016/j.carbon.2024.119651
Handle: http://hdl.handle.net/1942/44548

Boron-doped diamond decorated with metal-organic framework-derived compounds for high-voltage aqueous asymmetric supercapacitors

Shuling Liao[a], Chong Peng[a], Jifeng Zou[a], Soumen Mandal[b], Oliver A. Williams[b], Xinyi Huang[a], Mingwei Zhao[a], Jing Xu[c], Nianjun Yang[d,*], Siyu Yu[a,*]

[a] School of Chemistry & Chemical Engineering, Southwest University, Chongqing, China

[b] School of Physics and Astronomy, Cardiff University, Cardiff CF24 3AA, United Kingdom

[c] College of Materials and Metallurgy, Guizhou University, Huaxi District, Guiyang 550025, China

[d] Department of Chemistry & IMO–IMOMEC, Hasselt University, Diepenbeek 3590, Belgium

*Corresponding authors.

E-mail address: nianjun.yang@uhasselt.be; yusiyu@swu.edu.cn

Abstract

Conductive diamond has been recognized as a promising electrode material for supercapacitors due to its excellent stability and broad electrochemical potential window. To enhance the performance of diamond-based supercapacitors, this study focuses on two key strategies: incorporating redox-active species on the electrodes and/or in the electrolytes to increase the capacitance, and constructing asymmetric supercapacitors to expand the operating voltage range. In this context, pseudocapacitive Co_3O_4@boron doped diamond (BDD) and Bi-Bi_2O_3@BDD were synthesized using metal-organic framework (MOF) decorated BDD of Co-MOF@BDD and Bi-MOF@BDD as precursor materials, respectively. An aqueous asymmetric supercapacitor was then assembled using a pseudocapacitive electrode/redox electrolyte system of Co_3O_4@BDD | 3.0 M KOH+0.05 M $K_3Fe(CN)_6/K_4Fe(CN)_6$ as the positive compartment, and Bi-Bi_2O_3@BDD | 3.0 M KOH as the negative compartment. The resulting device demonstrated a wide operating voltage of 1.7 V, a maximal energy density of 10.0 Wh L^{-1} at a power density of 333.2 W L^{-1}. The remarkable performance can be attributed to the Faradaic redox reactions involving $[Fe(CN)_6]^{3-/4-}$, Co^{3+}/Co^{4+}, $Bi^0/Bi^{2+}/Bi^{3+}$ in the electrode materials and electrolytes. This work presents a novel way for fabricating aqueous supercapacitors with high voltage, high energy and power densities, offering significant potential for various energy storage applications.

Keywords: asymmetric supercapacitor, boron-doped diamond, MOF-derived compound, redox-active electrolyte

1 Introduction

Supercapacitors (SCs), as one of the most promising candidates for electrochemical energy storage, have attained growing interests and been applied in various areas in recent years [1, 2]. Depending on charge storage mechanisms, SCs can be divided into electrical double layer capacitors (EDLCs), pseudocapacitors (PCs), and redox-electrolyte enhanced SCs (R-SCs) [3]. An EDLC stores charges *via* a non-faradaic process, where the charges adsorb/accumulate electrostatically at the electrode/electrolyte interfaces. For PCs and R-SCs, reversible faradaic reactions take place, bringing additional pseudocapacitance and redox-electrolyte induced capacitance (R-capacitance), respectively. In general, PCs and R-SCs are able to deliver higher capacitances and higher energy densities than EDLCs. The difference between PCs and R-SCs lies in the location of redox-active species added, which are immobilized on electrodes for PCs and dissolved in confined electrolytes for R-SCs. Hence, to develop SCs with high performance, the employment of novel electrode materials and electrolytes are highly required.

Conductive diamond, especially boron doped diamond (BDD) has been regarded as one promising electrode material for SC applications. This is because a heavily boron-doped diamond demonstrates metal-like conductivity. Compared to other sp^2 carbon materials, the sp^3 conductive diamond possesses outstanding mechanical hardness, chemical inertness, and exceptional stability with maintained structure even under severe environmental and operational conditions (e.g., acidic or alkaline environments, high voltages and currents, and elevated temperatures). Moreover, BDD offers a wide electrochemical potential window, reaching up to 3.2 V in aqueous electrolytes and 4.6 V in organic electrolytes [4]. Additionally, diamond has diverse surface terminations and rich surface chemistry, which allows for controllable surface wettability and facilitates the loading of various pseudocapacitive materials. However, one shortcoming of a flat BDD electrode is its relatively low capacitance (3.6 - 7 μF cm^{-2} in 1.0 M Na_2SO_4) [5]. To solve this problem, several strategies have been proposed, namely the growth of diamond micro-/nanostructures with enlarged surface area using bottom-up overgrowth and top-down etching techniques, the formation of diamond hybrid materials by the combination of diamond with other sp^2 carbon materials, and the

synthesis of diamond pseudocapacitive composites by decorating pseudocapacitive materials on the surface of diamond [6]. The incorporation of pseudocapacitive materials (e.g., metal derived compounds and conducting polymers) yields a significant boost in capacitance. For example, by electrodeposition of MnO_2 on the surface of a flat BDD, a capacitance of 7.82 mF cm^{-2} was achieved at a scan rate of 10 mV s^{-1} in a 1.0 M Na_2SO_4 solution [5]. However, a 34% drop of the initial capacitance was observed for the MnO_2/BDD electrode after 1000 consecutive charging/discharging cycles at 100 mV s^{-1}. A Mn ion implanted BDD film was synthesized by Mn ion implantation into the BDD film at a high dose (10^{15}–10^{17} ions cm^{-2}), followed by a post-annealing treatment at 750 °C [7]. The Mn-BDD electrode could deliver a capacitance of 0.16 mF cm^{-2} at 1 mV s^{-1} in a 1.0 M Na_2SO_4 aqueous solution. A Ni/porous BDD film was fabricated through electrodeposition of Ni nanoparticle on a flat BDD film, followed by hydrogen-argon plasma etching with Ni nanoparticles as catalysts [8]. As a pseudocapacitive electrode, its capacitance reached 9.55 mF cm^{-2} at 5 mV s^{-1} in a 0.1 M Na_2SO_4 aqueous solution. Another $Ni(OH)_2$/BDD nanowires electrode was prepared through a two-step process: the deposition of a nickel metal layer on BDD nanowires *via* sputtering and the anodization of the Ni/BDD nanowires in NaOH solution [9]. This material demonstrated a high capacitance of up to 91 mF cm^{-2} at 5 mV s^{-1} in a NaOH aqueous solution, mainly due to the reversible redox reactions occurring between the nickel hydroxide and oxy-hydroxide groups. Nevertheless, the enhancement of capacitance by introducing pseudocapacitive electrode materials is accompanied by a considerable reduction in the operational potential windows, consequently limiting the energy density of associated SC devices [10]. One effective strategy to address this issue is the construction of asymmetric SCs (ASCs), which involves the utilization of distinct cathodic and anodic electrode/electrolyte systems possessing different potential windows [11].

Among various pseudocapacitive materials, cobalt oxide and bismuth oxide have emerged as promising choices for positive and negative electrode materials, respectively, owing to their low cost, environmental friendliness, high theoretical capacitances and abundant resources [12, 13]. To achieve high actual capacitances of these materials, they should exhibit high surface areas, remarkable amounts of exposed electrochemically active sites, and a porous structure that facilitates ion diffusion. However, achieving controllable

growth of metal oxides presents a persistent challenge. Recently, metal-organic frameworks (MOFs) have demonstrated efficacy as templates for the fabrication of metal oxides with large surface areas, adducible porous structure and controlled shapes [14]. MOFs are formed by coordinating organic molecules to metal ions/clusters. By varying the organic species and metal-contained units, a wide variety of MOF can be synthesized, each with unique properties in surface areas, porosity, and redox activity [15]. Under heat treatment, MOFs easily undergo decomposition, leading to the formation of metal oxides and other metal-containing compounds while preserving their structures. To the best of our knowledge, the synthesis of BDD decorated with MOF-derived oxides and their application as SC electrodes have not been reported up to now.

As another key component in the fabrication of SCs, the introduction of redox-active species into the electrolytes results in the formation of R-SCs [16]. Charges are stored through the diffusion-controlled redox reactions of these species at the surface or inside the porous cavity of the electrodes. In addition to the enhanced capacitance, R-SCs also show advantages of facile preparation and a full use of the selected electrodes [17]. For ASCs, achieving performance balance between positive and negative electrode/electrolyte systems is attainable by simply adjusting the type and concentration of dissolved redox species. Given the diverse redox potentials of various redox species, it is essential to select suitable ones to satisfy the working potential windows of related electrodes.

In the present study, a BDD ASC was constructed by employing BDD coated with Co_3O_4 derived from Co-MOF as the positive electrode, and BDD decorated with Bi-MOF derived Bi-Bi_2O_3 as the negative electrode **(Fig. 1)**. A redox electrolyte of 3.0 M KOH + 0.05 M $K_3Fe(CN)_6$/$K_4Fe(CN)_6$ and an inert electrolyte of 3.0 M KOH were used as the catholyte and anolyte, respectively. Its performance has been systematically investigated. The proposed concept provides a new way for the construction of diamond based aqueous SCs with a large operating voltage.

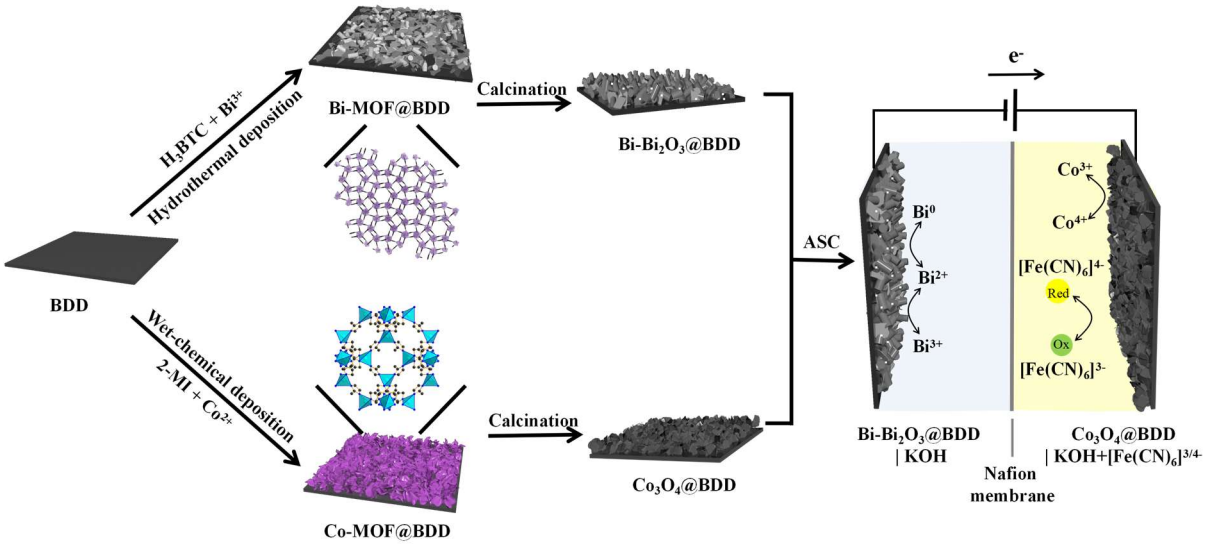

Fig. 1 Schematic illustration for the fabrication of an ASC using BDD decorated with metal-organic framework-derived compounds.

2 Experimental

2.1 Preparation of electrode materials

BDD films were grown on Si (100) wafers (2 inch) via microwave plasma assisted chemical vapor deposition technique. The deposition was conducted at a constant gas pressure of 45 Torr and a temperature of 800 ℃. A gas mixture with a flow rate of 300 sccm (standard cubic centimeter per minute) containing CH_4, H_2 and trimethylborane (B/C = 12821 ppm) was used as the main precursor. Trimethylborane was added during the growth process as the boron source. The charge carrier concentration was estimated to be 3.7×10^{21} cm^{-3} [18]. For further experiments, BDD films were immersed in a mixture of H_2SO_4 and HNO_3 with a volume ration of 3:1 for 60 min, then cleaned in deionized water using ultrasound, and finally dried in a N_2 atmosphere to change their wettability.

To coat BDD with Co_3O_4 films, Co-MOF was first synthesized and immobilized on BDD films. Here BDD samples were immersed in a mixed solution prepared by adding a 0.4 M 2-methylimidazole (2-MI) aqueous solution (15 mL) into a 0.05 M $Co(NO_3)_2 \cdot 6H_2O$ aqueous solution (15 mL). The deposition process was carried out at a temperature of 25°C, employing varying reaction times (t_i) of 15, 30, 45 and 60 min. After that, the BDD samples modified with Co-MOF was taken out, rinsed with deionized water, dried at 60 ℃ in air for 1 h, and

then annealed in air at 300 ℃ for 2 h to form Co_3O_4@BDD.

Bi-MOF was synthesized on the surface of BDD *via* a hydrothermal method, using $Bi(NO_3)_3$ $5H_2O$ as the bismuth source and 1,3,5-benzenetricarboxylic acid (H_3BTC) as the ligand. It was then utilized as the precursor, and calcined at high temperature to obtain Bi-Bi_2O_3@BDD. In detail, 0.75 g H_3BTC and 0.15 g $Bi(NO_3)_3$ $5H_2O$ were dissolved in 60 mL CH_3OH ultrasonically to form a transparent solution. Subsequently, it was transferred to a 100 mL autoclave preloaded with BDD, where the hydrothermal reaction was conducted at 120 ℃ for 1 h. After the reaction, BDD loaded with Bi-MOF was taken out once the autoclave was cooled to room temperature. It was washed with deionized water, dried in oven at 60 ℃ for 1 h, and finally subjected to calcination in a tubular furnace at 700 ℃ (heating rate: 5 ℃ min^{-1}) for 1 h under nitrogen atmosphere to obtain Bi-Bi_2O_3@BDD.

2.2 Characterization

The morphology and structure of prepared samples were investigated with field emission scanning electron microscopy (FE-SEM, Hitachi SU8010) and transmission electron microscopy (TEM, JEOL JEM-F200). For TEM examination, the Co_3O_4 nanostructures were collected from BDD substrate by mechanical scratching, and then dispersed ultrasonically in ethanol. After that, several drops of ethanol containing Co_3O_4 nanostructures were dropped on a copper grid, and dried in air. The chemical element analysis was conducted by energy dispersive X-ray spectroscopy (EDX, Hitachi SU8010). X-ray photoelectron spectroscopy (XPS, Thermo Scientific K-Alpha) with an Al Kα radiation was employed to investigate the elemental compositions and chemical states of the prepared films. The XPS spectra were analyzed using Thermo Scientific Avantage software. The binding energies (BEs) were calibrated by reference to the C 1s (284.80 eV) signal. The Raman spectra of Co_3O_4@BDD films were recorded on a Renishaw inVia Confocal Raman spectrometer, using a solid-state laser at 532 nm as the excitation source. The XRD patterns of collected sample powders were recorded using a Rigaku Ultma IV X-Ray diffractometer or an XD-6 X-Ray diffractometer with Cu Kα radiation.

2.3 Electrochemical measurements

Electrochemical measurements were carried out on a CHI760E electrochemical workstation (Shanghai Chenhua Inc., China). A standard three-electrode system was firstly employed to examine the electrochemical performance of Co_3O_4@BDD and Bi-Bi_2O_3@BDD films, where an Ag/AgCl (3.0 M KCl) electrode was used as the reference electrode and a coiled Pt wire as the counter electrode. Aqueous solutions of 3.0 M KOH and 3.0 M KOH + 0.05 M $K_3Fe(CN)_6$/$K_4Fe(CN)_6$ were utilized as the electrolytes. Two-electrode ASC devices were assembled using Co_3O_4@BDD | 3.0 M KOH with/without 0.05 M $K_3Fe(CN)_6$/$K_4Fe(CN)_6$ and Bi-Bi_2O_3@BDD | 3.0 M KOH as the positive and negative compartments, respectively. A Nafion® membrane (Alfa Aesar) was employed as the separator. The effective area of used capacitor electrodes was 0.05 cm^2. Cyclic voltammograms (CV) at different scan rates, galvanostatic charging/discharging (GCD) curves at different current densities, and Nyquist plots at open circuit potentials over a frequency range from 1 Hz to 1 MHz with a small amplitude of 5 mV were recorded for different SCs. The specific capacitances (C, F cm^{-2}), energy densities (E, Wh L^{-1}), and power densities (P, W L^{-1}) were calculated according to the reported methods [19-21].

3 Results and discussion

3.1 Characterization

The SEM image of a BDD film is shown in **Fig. S1a.** A Co-MOF film was then deposited on BDD film *via* the reaction of a metal source of $Co(NO_3)_2 \cdot 6H_2O$ and a ligand of 2-methylimidazole. Considering that the highest capacitance was obtained on Co_3O_4@BDD electrodes synthesized with a t_i of 45 min (see following section), the characterization was focused on these samples. As shown in **Fig. S1b**, Co-MOF with a 2D sheet-like form has been coated uniformly on the surface. The XRD pattern of the Co-MOF in **Fig. S1c** confirms the formation of Co-ZIF, which matches well with ZIF-L crystals [22-24]. After thermal treatment of the Co-MOF@BDD film at 300 ℃ in air for 2 h, the MOF precursor has been decomposed and oxidized with a release of gas molecules, leading to the formation of Co_3O_4 film in flower-like structure with thinner and rougher nanosheets (**Fig. 2a**). Such a morphology brings large specific surface area of the film and allows facilitated electrolyte penetration and

electron transfer. The inset image in **Fig. 2a** presents the cross section of the Co_3O_4@BDD film, where Co_3O_4 and BDD are both uniformly deposited with regular section. The thicknesses of the BDD and Co_3O_4 layers were measured to be about 2.0 and 2.5 μm, respectively. Furthermore, the full removal of N element during the thermal treatment of Co-MOF@BDD is confirmed by comparing the EDX spectra collected from Co_3O_4@BDD film (**Fig. 2b**) and Co-MOF@BDD precursor (**Fig. S1d**), indicating the full transformation of Co-MOF. The EDX element mapping of the Co_3O_4@BDD film (**Fig. 2c-f**) demonstrates uniform distributions of the component elements, including C, O and Co, throughout the film.

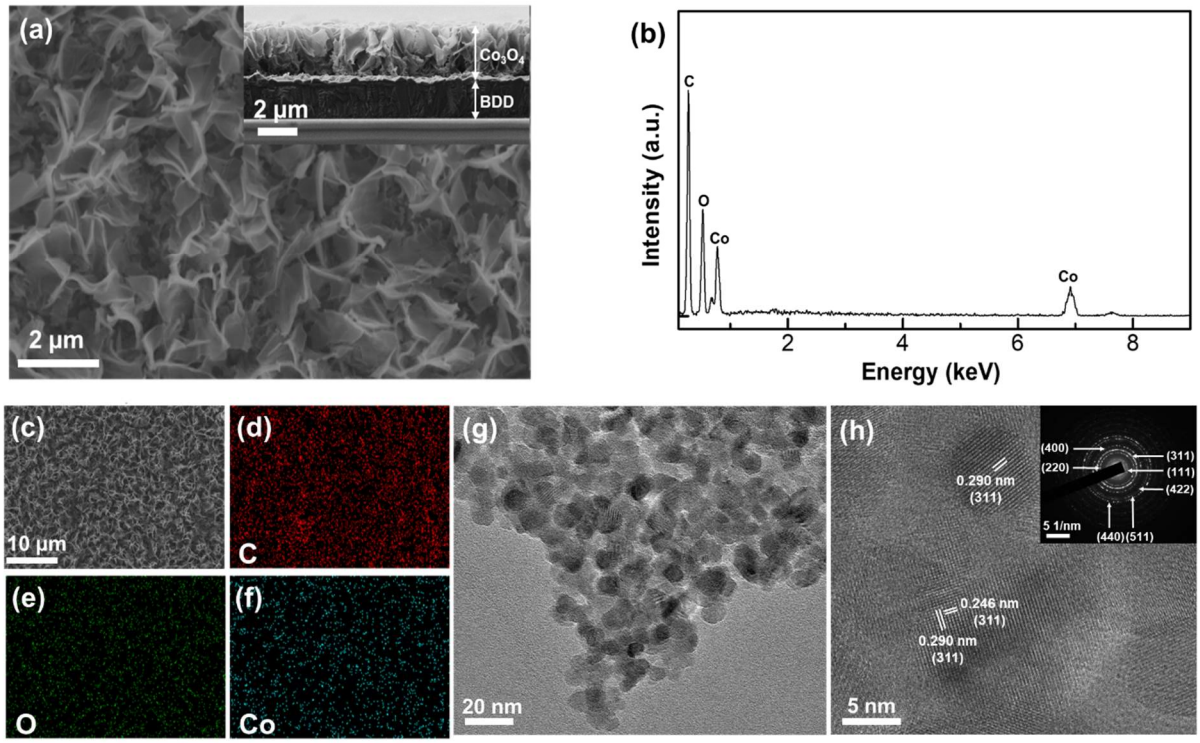

Fig. 2 (a) FE-SEM image, (b) EDX spectrum and (c-f) EDX element mapping of Co_3O_4@BDD films. The inset image in (a) shows the cross-section of the film. (g) TEM image and (h) HRTEM image of Co_3O_4 nanostructures. The inset image in (h) shows SAED pattern of Co_3O_4.

The TEM image in **Fig. 2g** reveals that Co_3O_4 nanosheets are composed of aggregated nanoparticles with particle size of about 10 nm. Nano-sized pores are found at the grain boundaries, providing interconnected ion diffusion pathways with reduced length, leading to facilitated ion transport and enhanced charge storage. The high-resolution TEM (HRTEM)

image of Co_3O_4 (**Fig. 2h)** shows clear lattice fringes with interplanar spacing of 0.290 and 0.246 nm, corresponding to the (220) and (311) planes of Co_3O_4 [25, 26]. The selected area electron diffraction (SAED) pattern presented in the inset of **Fig. 2h** are used to examine the crystalline nature of Co_3O_4 nanostructure. The presence of discontinuous diffuse rings in SAED pattern indicates the polycrystalline nature of Co_3O_4.

XPS measurements were carried out to investigate the atomic composition and the chemical states of a prepared Co_3O_4@BDD film. Its XPS survey spectrum **(Fig. 3a**) shows the presence of C, O and Co elements in the sample. The absence of peaks corresponding to nitrogen further confirms the removal of this element during the thermal treatment of the Co-MOF@BDD film. The high-resolution XPS spectrum of O 1s core level (**Fig. 3b**) is deconvoluted into three peaks. The major peak at the lowest BE of 529.8 eV is associated with the Co-O bonding in the Co_3O_4 phase [27, 28]. The high-resolution XPS spectrum of Co 2p core level is presented in **Fig. 3c**. Two main peaks are observed at BEs of 794.7 and 779.7 eV, with a spin-energy separation of 15 eV. Each peak is accompanied by a shakeup satellite. These two peaks are assigned to Co $2p_{1/2}$ and $2p_{3/2}$ states, respectively, which are typical characteristics of a Co_3O_4 phase [29, 30]. Upon deconvolution of the Co 2p XPS spectrum, the peaks centered at 794.7 and 779.7 eV correspond to the Co^{3+} state, while those located at 796.5 and 781.3 eV are assigned to the Co^{2+} state [31, 32]. In the Raman spectrum of a Co_3O_4@BDD film (**Fig. 3d**), four obvious peaks located at around 467, 508, 603 and 669 cm^{-1} are assigned to the E_g, F_{2g}^1, F_{2g}^2, and A_{1g} modes of Co_3O_4 crystalline phase, respectively, similar as those reported in literature [33, 34]. The band centered at approximately 669 cm^{-1} (A_{1g} mode) is attributed to the characteristics of the octahedral CoO_6 sites. Compared to bulk Co_3O_4, the peak positions of the four Raman-active modes observed here exhibit a downward shift to lower wavenumbers by approximately 14 – 22 cm^{-1} [35]. This is because of the optical phonon confinement effect that occurs in nanostructures and structural defects, resulting in uncertainty of the phonon wave vectors and consequently a downshift of the Raman peaks [36]. Besides, the peak detected at around 1328 cm^{-1} with low intensity corresponds to the first-order Raman mode of diamond substrate [37].

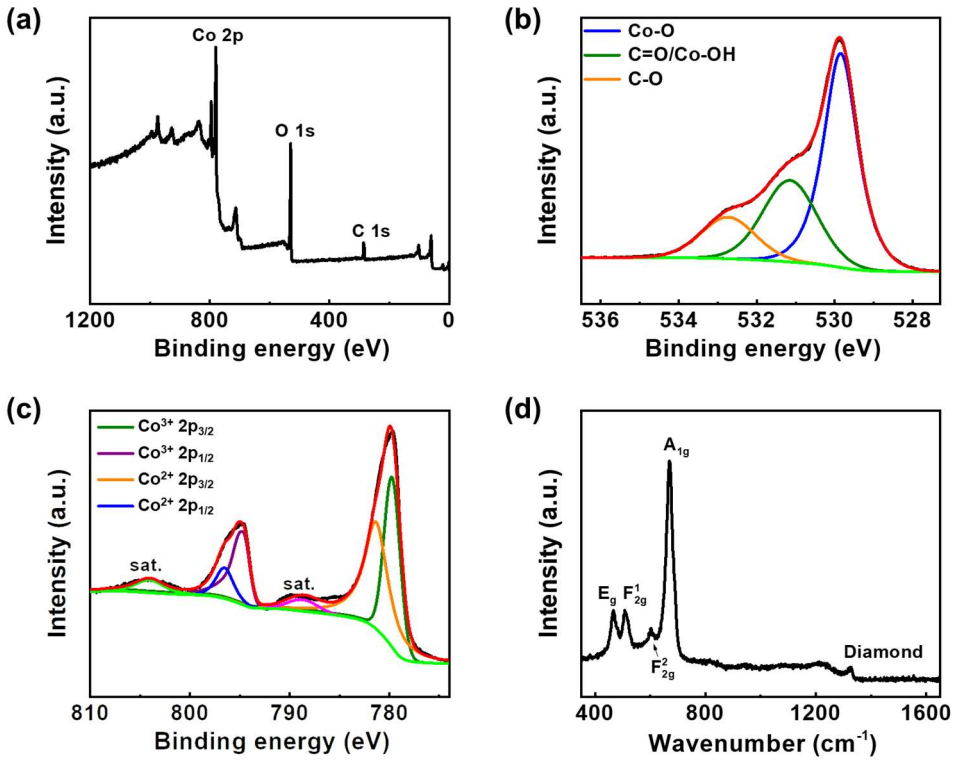

Fig. 3 (a) XPS survey spectrum, (b, c) high resolution XPS spectra of (b) O 1s and (c) Co 2p core levels, and (d) Raman spectrum of Co_3O_4@BDD films.

According to the FE-SEM image of Bi-MOF@BDD (**Fig. 4a**), Bi-MOF exhibits a hexagonal rod structure with smooth surface, accompanied by the presence of nanosheets. After calcination at high temperature in nitrogen atmosphere, the obtained Bi-Bi_2O_3 still maintains the morphology of Bi-MOF (**Fig. 4b**). The densely distributed particles observed on the surface of Bi-Bi_2O_3@BDD might be elemental Bi. The interweaving of rod-like and sheet-like structures in Bi-Bi_2O_3 leads to the formation of a three-dimensional network with continuous pores, facilitating the transport of charged particles. Additionally, the presence of the metallic bismuth effectively enhances the conductivity of the material, and provides rich active sites for electrochemical processes. The thicknesses of BDD and Bi-Bi_2O_3 layers were measured to be approximately 2.0 μm and 37.9 μm, respectively (inset image in **Fig. 4b**). According to EDX elemental mapping images of Bi-Bi_2O_3@BDD film (**Fig. 4c-f**), the elements C, O and Bi are uniformly distributed throughout the film. The presence of carbon in Bi-Bi_2O_3 suggests that during the pyrolysis of Bi-MOF, some organic ligands were transformed into carbon materials and deposited within the film layer. The formation of

carbon materials is beneficial for improving the conductivity and stability of the material [38].

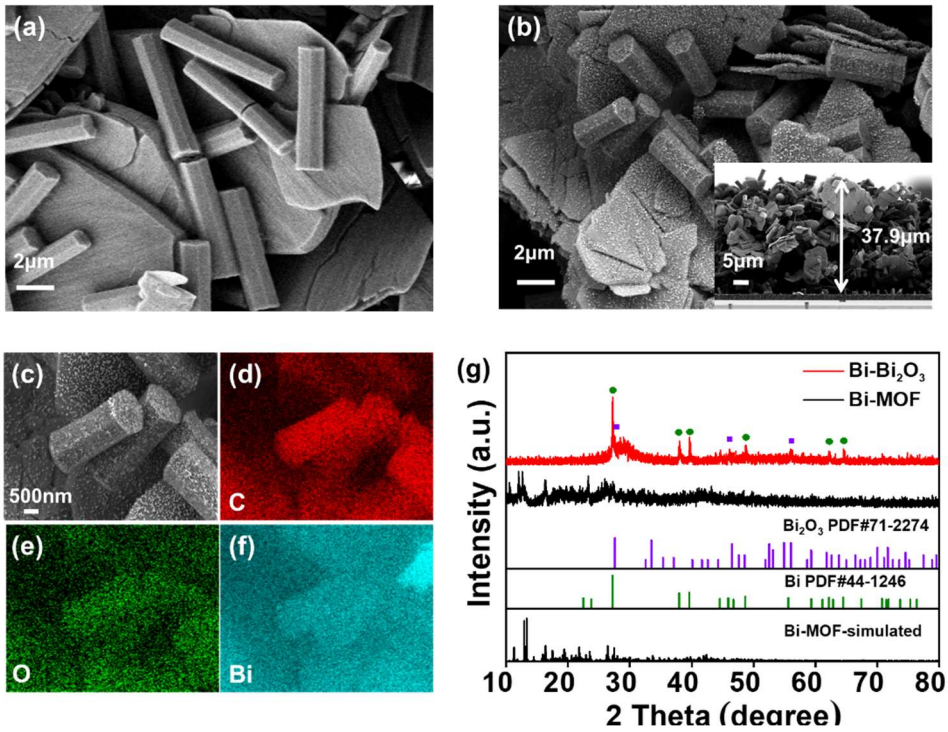

Fig. 4 FE-SEM images of (a) Bi-MOF@BDD and (b) Bi-Bi_2O_3@BDD. The inset image in (b) shows the cross-section of Bi-Bi_2O_3@BDD. (c) FE-SEM image and (d-f) corresponding EDX elemental mapping images of Bi-Bi_2O_3@BDD. (g) XRD patterns of Bi-MOF and Bi-Bi_2O_3.

The XRD patterns of Bi-MOF and Bi-Bi_2O_3 are shown in **Fig. 4g**. The characteristic peaks in the XRD pattern of Bi-MOF align well with the simulated XRD pattern of CAU-17 Bi-MOF [39], confirming the successful synthesis of Bi-MOF precursor. In the XRD pattern of Bi-Bi_2O_3, peaks located at 27.2°, 38°, 39.6°, 48.7°, 62.2° and 64.5° can be attributed to (012), (104), (110), (202), (116) and (122) crystal planes of Bi (PDF# 44-1246), while peaks centered at 28°, 46.3°, and 54.8° correspond to (012), (041), and (-241) crystal planes of Bi_2O_3 (PDF# 44-1246). The broad peak observed between 26.5 - 30° corresponds to carbon [40]. This result confirms the presence of Bi, Bi_2O_3 and carbon in the derived product of Bi-MOF, consistent with SEM results.

The atomic composition and chemical states of Bi-Bi_2O_3@BDD film were analyzed by XPS. Its XPS survey spectrum (**Fig. 5a**) indicates that the sample consists of elements C, O, and Bi. In the high-resolution XPS spectrum of Bi 4f (**Fig. 5b**), four characteristic peaks corresponding to the two oxidation states of Bi^{3+} and Bi^{2+} can be obtained by fitting the two

recorded peaks at 158.8 and 164.1 eV. The deconvoluted peaks at 164.6 and 159.3 eV correspond to Bi^{3+} $4f_{5/2}$ and Bi^{3+} $4f_{7/2}$, respectively, while those appearing at 164.0 and 158.7 eV are attributed to Bi^{2+} $4f_{5/2}$ and Bi^{2+} $4f_{7/2}$, respectively [38]. Besides, the peaks measured at 162.1 and 156.8 eV are assigned to Bi^{0} $4f_{5/2}$ and Bi^{0} $4f_{7/2}$, respectively [41]. The high-resolution XPS spectrum of C 1s in **Fig. 5c** can be deconvoluted into three peaks located at 284.8, 286.1 and 289.5 eV, corresponding to the C-C, C-O and O-C=O bonds, respectively. In the high-resolution XPS spectrum of O 1s (**Fig. 5d**), the fitted peaks at 529.6, 532.0 and 533.7 eV can be ascribed to Bi-O, C-O and O-C=O bonds, respectively [42-45].

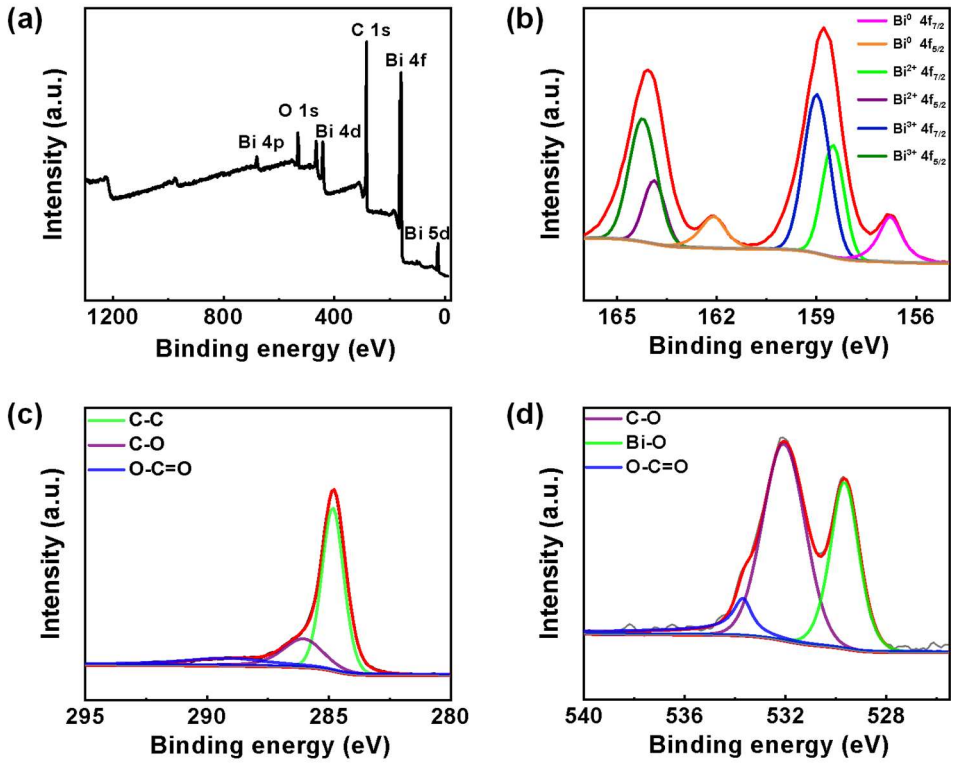

Fig. 5 XPS spectra of Bi-Bi_2O_3@BDD: (a) survey spectrum, high-resolution spectra of (b) Bi 4f, (c) C 1s, and (d) O 1s.

3.2 Electrochemical performance

3.2.1 Electrochemical performance of Co_3O_4@BDD

The electrochemical performance of Co_3O_4@BDD electrodes synthesized with different t_i of 15 – 60 min was evaluated and compared, by recording their CVs in 3.0 M KOH aqueous electrolyte in a potential window of 0 - 0.5 V (*vs*. Ag/AgCl) at a scan rare of 100 mV s^{-1} (**Fig. 6a**). One pair of apparent anodic and cathodic peaks at ca. 0.4 and 0.36 V (*vs*. Ag/AgCl),

respectively, are observed in all CV curves, representing the reversible surface faradaic reactions between different valance states of cobalt associated with OH^- [46]:

$$Co_3O_4 + OH^- + H_2O \leftrightarrow 3CoOOH + e^- \quad (1)$$

$$CoOOH + OH^- \leftrightarrow CoO_2 + H_2O + e^- \quad (2)$$

The slight shifts in the redox peaks of these CVs are attributed to variations in the loading amount of Co_3O_4, which influence the ion/electron transfer rates, the reaction kinetics, and the current response during the cyclic voltammetry test. Compared to the CV of a BDD film measured under the same conditions (**Fig. 6a**), the CV of the BDD electrode is displayed as a line, indicating a significant improvement of the capacitance by immobilizing pseudocapacitive Co_3O_4 on BDD. The highest peak currents and capacitive currents are observed on the Co_3O_4@BDD electrode with t_i of 45 min, an indication of its highest performance. The decrease of the current intensity in case of a t_i of 60 min might be due to the relatively poor conductivity of the metal oxides. Such phenomena was also observed on MnO_2 coated BDD electrodes [5]. Therefore, the Co_3O_4@BDD electrode with t_i of 45 min has been selected for further SC application. Its CVs recorded in 3.0 M KOH are illustrated in **Fig. S2a**. Small shifts in redox peaks are observed in CVs at different scan rates, which is mainly due to polarization effects [47]. At lower scan rates, the redox reaction is given sufficient time to reach equilibrium, resulting in relatively weak polarization. Conversely, as the scan rate increases, the reaction kinetics are challenged to match the rapid changes in potential, leading to enhanced polarization effects, which in turn affect the specific positions of the redox peaks. Here, with the increase of the scan rate from 20 to 100 mV s^{-1}, the potential separation between the redox peaks increases from 0.021 to 0.05 V. Such a small change in the potential separation demonstrates the good reaction kinetics on the electrode. Meanwhile, the corresponding GCD curves (**Fig. S2b**) at different current densities are non-linear with plateaus in the charging and discharging sections, confirming the redox reaction of Co_3O_4. The specific capacitance increases with the decrease of the applied current densities, namely 22.6, 26.8, 30.2 and 33.2 mF cm^{-2} at 10, 5, 3, and 2 mA cm^{-2}, respectively. These values are about three orders of magnitude higher than that of a flat BDD electrode [6]. This is mainly due to the additional pseudocapacitance provided by the Co_3O_4 film with porous structure and enlarged surface area.

To further improve the performance of Co_3O_4@BDD based PC, a pair of redox species of 0.05 M $K_3Fe(CN)_6/K_4Fe(CN)_6$ was introduced in 3.0 M KOH aqueous solution for the construction of a R-SC. The faradaic redox reaction of $Fe(CN)_6^{3-/4-}$ during the charging/discharging processes is expected to contribute additional R-capacitance [3]. **Figure S2c** illustrates the recorded CVs at scan rate of 20 to 100 mV s^{-1} within a potential window of 0 - 0.5 V (*vs*. Ag/AgCl)，where a broad oxidation peak (ca. 0.4 V *vs*. Ag/AgCl) and a reduction peak (ca. 0.26 V *vs*. Ag/AgCl) are observed. These peaks refer to the redox reactions of $Fe(CN)_6^{3-/4-}$ in the electrolyte and Co_3O_4 coated on the electrode surface. The CV of the R-SC is compared to the theoretical CV, in which the currents are calculated by the direct sum of the CV currents recorded on Co_3O_4@BDD based PC in 3.0 M KOH, and BDD based R-SC in 3.0 M KOH + 0.05 M $K_3Fe(CN)_6/K_4Fe(CN)_6$, under a fixed scan rate of 100 mV s^{-1} (**Fig. 6b**). The anodic and cathodic peaks in the tested CV cover those of Co_3O_4 and $Fe(CN)_6^{3-/4-}$, and the peak intensities are also stronger. Furthermore, the integrated area of the CV tested is quite higher than that of the CV calculated. Therefore, the coated Co_3O_4 film not only provides extra pseudocapacitance, but also promotes synergistically the redox reaction of $Fe(CN)_6^{3-/4-}$. The shape of GCD curves (**Fig. S2d and Fig. 6c**) further prove the involvement of redox reactions, which is in agreement with those observed on CVs. At the current density of 5 mA cm^{-2}, the discharging time of Co_3O_4@BDD obtained in KOH + $K_3Fe(CN)_6/K_4Fe(CN)_6$ is about 5 times as high as that obtained in KOH solution (**Fig. 6c**). According to the GCD curves, the capacitances of Co_3O_4@BDD based R-SC were calculated to be 54.0, 65.7, 86.0 and 138.5 mF cm^{-2} at 20, 15, 10, and 5 mA cm^{-2}, respectively, much larger than those of the Co_3O_4@BDD PC. The Nyquist plots of a Co_3O_4@BDD film in the inert solution of 3.0 M KOH and in the redox electrolyte of 3.0 M KOH + 0.05 M $Fe(CN)_6^{3-/4-}$ were recorded at open circuit potentials and compared (**Fig 6d**). After adding redox species to the electrolyte, the internal resistance increases from 4.4 to 4.7 Ω, whereas the charge transfer resistance decreases from 21.4 to 12.7 Ω, leading to an 8.4 Ω reduction in the overall impedance. The slight increase in internal resistance might be due to the reduced transfer rate of the redox species inside the electrode pores. The significant decrease in charge transfer resistance indicates an accelerated electron transfer at the electrode/electrolyte interfaces after the introduction of redox species. Moreover, the Nyquist plot for the

Co_3O_4@BDD based R-SC exhibits a notably smaller slope in the low and medium frequency region compared to that for the Co_3O_4@BDD based PC, owing to a significant enhancement of the diffusion-controlled process. Furthermore, at low frequencies, the line in the Nyquist plot of the Co_3O_4@BDD based R-SC shows a slight deviation from a straight line. This might be attributed to the presence of an additional time constant, arising from the diffusion limitation of redox-active ions, especially within the narrow pores and internal channels of the electrode material [48, 49].

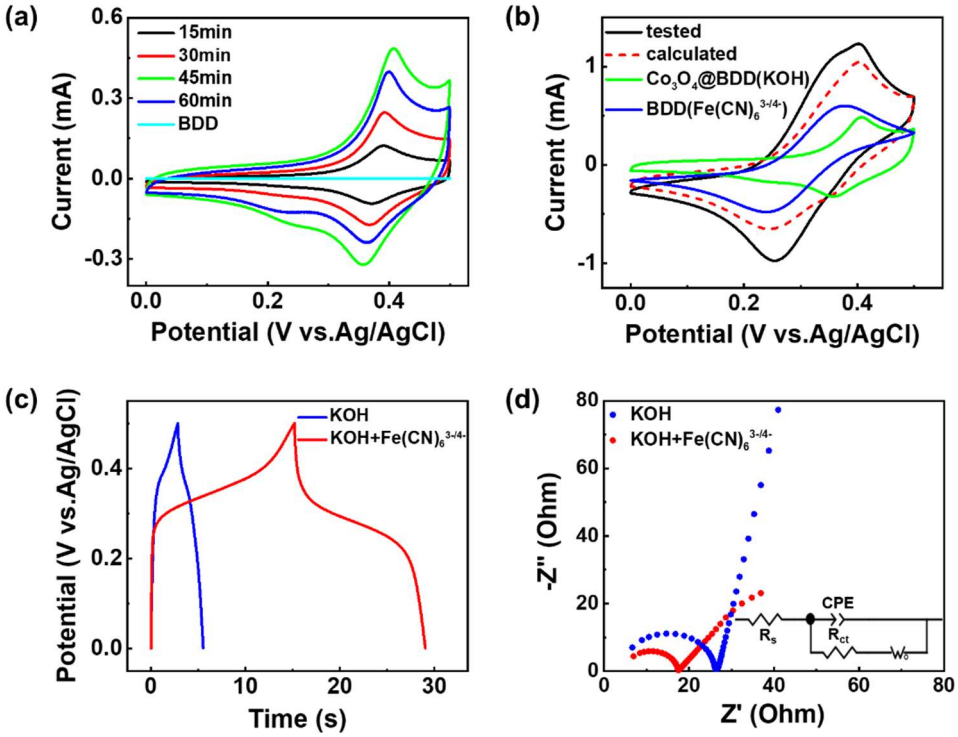

Fig. 6 (a) CVs of Co_3O_4@BDD films prepared with t_i of 15, 30, 45 and 60 min, as recorded at 100 mV s^{-1} in 3.0 M KOH aqueous solution. (b-d) Performance of Co_3O_4@BDD films with t_i of 45 min: (b) comparison of the CV tested in 3.0 M KOH + 0.05 M $Fe(CN)_6^{3-/4-}$ aqueous solution, and the theoretical CV calculated by the addition of the CV currents recorded on Co_3O_4@BDD/3.0 M KOH and BDD/3.0 M KOH + 0.05 M $Fe(CN)_6^{3-/4-}$ electrode/electrolyte systems, where the applied scan rate was 100 mV s^{-1}; comparison of (c) the GCD curves at 5 mA cm^{-2} and (d) Nyquist plots in different electrolytes. The inset in (d) shows the equivalent electric circuit for the analysis of Nyquist plots, where R_s denotes the internal resistance, R_{ct} the charge transfer resistance, W the Warburg impedance and CPE the constant phase element.

3.2.2 Electrochemical performance of Bi-Bi_2O_3@BDD

The electrochemical performance of Bi-Bi_2O_3@BDD electrode was evaluated in 3.0 M KOH aqueous solution using a three-electrode system. The selected potential window was -1.2 - 0 V (*vs*. Ag/AgCl). In CVs (**Fig. 7a**) recorded at different scan rates (10 - 100 mV s^{-1}), two oxidation peaks observed at about -0.61 and -0.45 V (*vs.* Ag/AgCl) are originated from the oxidation reactions of $Bi^0 \rightarrow Bi^{2+}$ (metastable phase) $\rightarrow Bi^{3+}$. Meanwhile, the reduction peaks located at around -1.0 and -0.8 V (*vs*. Ag/AgCl) are due to the reduction reactions of $Bi^{3+} \rightarrow Bi^{2+} \rightarrow Bi^0$. Therefore, Bi-$Bi_2O_3$@BDD exhibits typical pseudocapacitive behavior in KOH electrolyte. As the scan rate increases, the positions of these redox peaks shift slightly, which may be caused by the polarization effect of the electrode material [40, 50]. The Faraday redox reactions involving Bi^{3+}, Bi^{2+} and Bi^0 (**Eq. 3-5**) can contribute additional pseudocapacitance, thus significantly improving the electrochemical performance of BDD electrodes [51-53].

$$Bi_2O_3 + H_2O + 2e^- \leftrightarrow Bi_2O_2 + 2OH^- \quad (3)$$

$$Bi_2O_2 + 2H_2O + 4e^- \leftrightarrow 2Bi^0 + 4OH^- \quad (4)$$

$$\text{Total reaction: } Bi_2O_3 + 3H_2O + 6e^- \leftrightarrow 2Bi^0 + 6OH^- \quad (5)$$

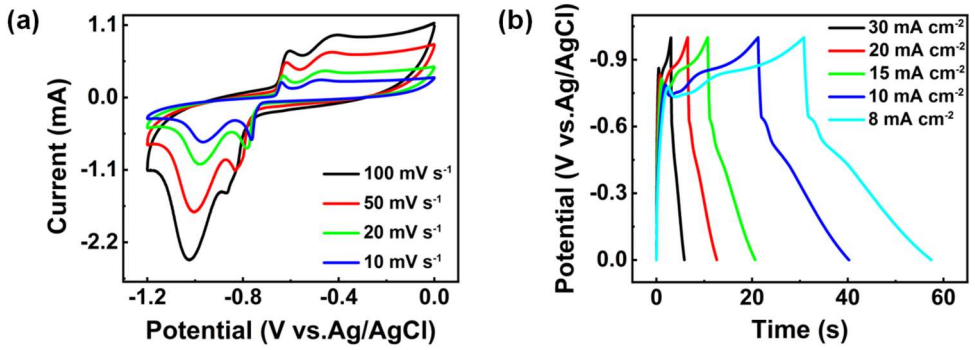

Fig. 7 Electrochemical performance of Bi-Bi_2O_3@BDD electrode in 3.0 M KOH aqueous solution: (a) CVs at different scan rates and (b) GCD curves at different current densities.

Fig. 7b shows the GCD curves of Bi-Bi_2O_3@BDD at various current densities. Plateaus related to the redox reactions of Bi^0/Bi^{2+} and Bi^{2+}/Bi^{3+} are evident in all curves, which pass well with the redox peaks in CVs. It should be noted that, sharp peaks are observed within the potential range of -0.7 to -0.9 V (vs. Ag/AgCl) in the GCD curves (**Fig. 7b**), corresponding to the sharp peaks observed at similar potentials in the CVs (**Fig. 7a**). The appearance of sharp

peaks instead of plateaus in the GCD curves can be attributed to the rapid and reversible nature of the electrochemical reactions taking place at the electrode surface. This facilitates a concentrated and immediate electron transfer during the redox process, leading to a sharp fluctuation in current within a narrow potential window. Similar phenomena have also been observed in the GCD curves of other Bi_2O_3 based electrodes [42, 50, 52, 54]. Based on the GCD curves, the capacitance of Bi-Bi_2O_3@BDD was calculated to be 84.6, 121.6, 148.5, 189.9 and 213.0 mF cm^{-2} at 30, 20, 15, 10 and 8 mA cm^{-2}, respectively. The high specific capacitance and good rate performance of Bi-Bi_2O_3@BDD may be attributed to the following factors: i) pseudocapacitive behavior of Bi-Bi_2O_3; ii) improved conductivity and active electrochemical sites due to presence of metallic Bi; iii) the three-dimensional porous structure of the film, facilitating mass transport and charge transfer during charging/discharging processes; iv) enhanced conductivity provided by carbon material deposited within Bi-Bi_2O_3, promoting rapid charge transfer.

3.2.3 Electrochemical performance of ASC devices

ASCs were fabricated using Co_3O_4@BDD and Bi-Bi_2O_3@BDD as the cathode and anode, 3.0 M KOH with/without 0.05 M $K_3Fe(CN)_6/K_4Fe(CN)_6$ and 3.0 M KOH as the cathodic and anodic electrolytes, respectively. The cathodic and anodic compartments were separated by a Nafion ion-selective membrane. These ASCs achieve a wide voltage window of 0 - 1.7 V, much higher than that provided by a symmetric supercapacitor of Co_3O_4@BDD | 3 M KOH | Co_3O_4@BDD (about 0.5 V) (**Fig. 8a, Fig. S3a and b**). The voltage window extension achieved by replacing one Co_3O_4@BDD electrode with Bi-Bi_2O_3@BDD is due to the distinct electrochemical potential windows of the electrodes in the KOH aqueous electrolyte: the Co_3O_4@BDD electrode operates within 0 – 0.5 V (*vs*. Ag/AgCl), while the Bi-Bi_2O_3@BDD electrode spans -1.2 – 0 V (*vs*. Ag/AgCl). However, in the ASC of Co_3O_4@BDD | KOH | Bi-Bi_2O_3@BDD, a mismatch between the Co_3O_4@BDD | KOH and the Bi-Bi_2O_3@BDD | KOH electrode/electrolyte systems is found, especially at scan rates higher than 20 mV s^{-1} (**Fig. S3b**). This issue was addressed by incorporating $[Fe(CN)_6]^{3/4-}$ redox species into the positive Co_3O_4@BDD electrode/electrolyte system (**Fig. 8a**). Additionally, the recorded CV currents for the redox electrolyte-enhanced ASC (R-ASC) are

higher than those without the redox species, indicating an enhanced capacitance after the addition of the redox species to the electrolyte. Several pairs of distinct redox peaks appear in the CV curves of the R-ASC at different scan rates ranging from 10 to 100 mV s^{-1}. They are caused by the Faraday reactions of redox-active species in the electrode materials and electrolytes ($[Fe(CN)_6]^{3-/4-}$, Co^{3+}/Co^{4+}, $Bi^0/Bi^{2+}/Bi^{3+}$) during the charging and discharging processes. Moreover, the shape of CV curves maintains well at all scan rates, indicating stable electrochemical behavior of the R-ASC.

Fig. 8b shows the GCD curves of the R-ASC at different current densities. At the current density of 10 mA cm^{-2}, the Coulombic efficiency reaches 95.1%. With increasing current density, the Coulombic efficiency of the R-ASC slightly decreases, and still maintains 85.4% at 1 mA cm^{-2}, demonstrating good reversibility of the device. In comparison, the ASC of Co_3O_4@BDD | KOH | Bi-Bi_2O_3@BDD exhibits relatively low Coulombic efficiencies at different current densities, with values of 82.3% at 10 mA cm^{-2} and 35.6% at 2 mA cm^{-2} (**Fig. S3c**). This discrepancy is attributed to an imbalance in charge storage between the positive and negative compartments. Moreover, the discharging durations of this ASC are quite smaller than those of the R-ASC at same current densities, demonstrating an increase in capacitance with the introduction of redox species to the electrolyte. The capacitance of the R-ASC was calculated to be 9.7, 13.4, 17.7, 22.8, and 32.0 mF cm^{-2} at current densities of 10, 5, 3, 2, and 1 mA cm^{-2}, respectively. Further calculations of the energy and power densities of the R-ASC device (**Fig. 8c**) reveal that at the power density of 333.2 W L^{-1}, the R-ASC achieves the maximum energy density of 10.0 Wh L^{-1}. When the power density increases to 3668.7 W L^{-1}, its energy density remains at 3.4 Wh L^{-1}. The significant decrease in power density concurrent with the increase in energy density might be attributed to the relatively high impedance of the entire system. To address this issue, the following strategies are worth exploring: developing porous electrode materials with enhanced electrical conductivity, selecting and designing innovative redox-active electrolytes that are more compatible with electrode materials, and engineering SC configurations with minimized dead space. Nevertheless, the energy and power densities are still larger than those of most BDD based SCs [55, 56]. Compared to other ASC devices based on Bi_2O_3 anodes and/or Co_3O_4 cathodes reported in literature, the ASC device assembled in this work demonstrates superior or

comparable energy and power densities (**Table S1**).

As a crucial factor for the practical application of the R-ASC, its cycling stability was evaluated using GCD technique at a current density of 20 mA cm^{-2} (**Fig. 8d**). After 1500 cycles, 89% of the initial capacitance remains, indicating the good stability of the R-ASC. The Nyquist plot of the R-ASC after the cycling test was examined and compared to that recorded before the test (**Fig. S4a**). The internal resistance of the device increases after the lifetime test, which might originate from changes in the chemical state and structure of the MOF-derived compounds, as well as a deterioration in electrode-electrolyte interactions. The XPS analyses of the negative and positive electrode materials were performed after the cyclic test. In the Co 2p XPS spectrum, the two prominent peaks corresponding to the Co $2p_{1/2}$ and $2p_{3/2}$ states have shifted to higher BE values of 795.1 and 780.0 eV, respectively (**Fig. S4b**). This demonstrates an increase in the proportion of the Co^{2+} oxidation state after 1500 charging/discharging cycles. The Bi 4f XPS spectrum reveals a decrease in the intensity of the peaks associated with Bi^0 (**Fig. S4c**), suggesting that a significant amount of elemental bismuth has been oxidized to a higher oxidation state.

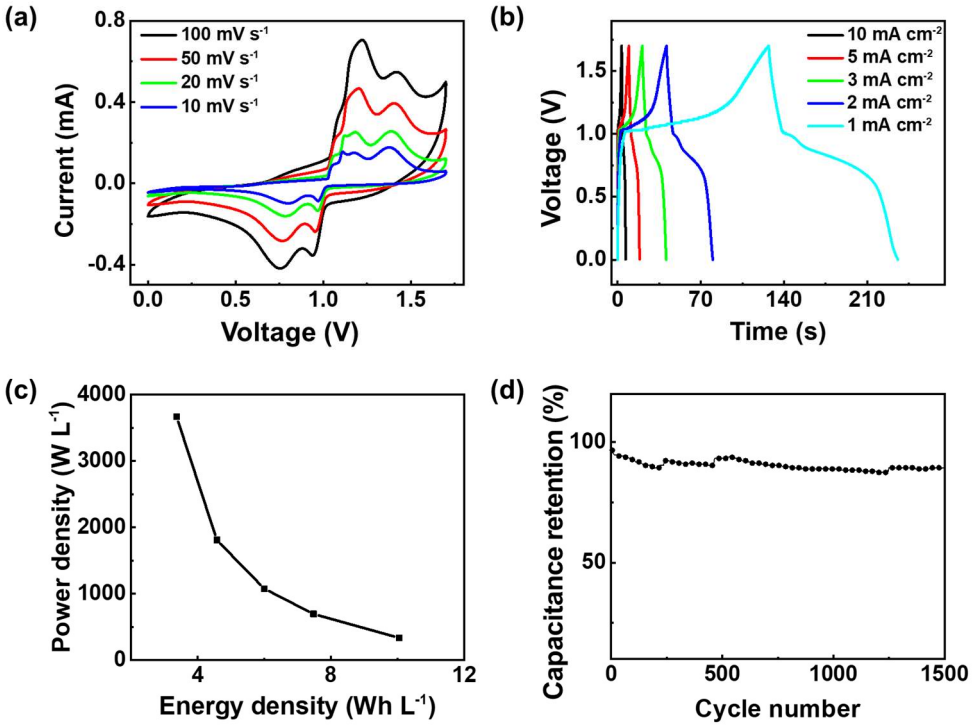

Fig. 8 Electrochemical performance of the R-ASC in a voltage window of 0 - 1.7 V: (a) CVs at different scan rates, (b) GCD curves at different current densities, (c) Ragone plot, and (d) capacitance retention at a current density of 20 mA cm^{-2}.

4 Conclusion

In this work, two pseudocapacitive electrodes were synthesized by decorating MOF-derived compounds on BDD. Co_3O_4@BDD was prepared by the thermal pyrolysis of Co-MOF@BDD. The Co_3O_4 film exhibited flower-like structure consisting of thin and rough nanosheets, which was beneficial for ion and electron transfer. By using redox-active electrolyte of 3.0M KOH + 0.05 M $K_3Fe(CN)_6/K_4Fe(CN)_6$, Co_3O_4@BDD showed a high capacitance of 138.5 mF cm^{-2} at 5 mA cm^{-2}. In Bi-Bi_2O_3@BDD obtained by the thermal pyrolysis of Bi-MOF@BDD, Bi-Bi_2O_3 possessed interweaved rod-like and sheet-like structures. The electrode could provide a capacitance of 213.0 mF cm^{-2} in 3.0 M KOH. An R-ASC device was designed and developed by employing Co_3O_4@BDD | 3.0 M KOH+0.05 M $K_3Fe(CN)_6/K_4Fe(CN)_6$ and Bi-Bi_2O_3@BDD | 3.0 M KOH as the positive and negative electrode/electrolyte systems, respectively. The device could be operated over a wide voltage window of 0 - 1.7 V. It achieved a maximal energy density of 10.0 Wh L^{-1} at a power density of 333.2 W L^{-1}, and a maximal power density of 3668.7 W L^{-1} at an energy density of 3.4 Wh L^{-1}. These values are higher or comparable to those of most BDD-based SCs, as well as ASCs using Bi_2O_3 anodes and/or Co_3O_4 cathodes. Therefore, this work provides a novel way for the construction of high-performance supercapacitors. It should be noted that the BDD used in this study is a flat diamond with a relatively low specific surface area, limiting the area available for depositing MOF-derived compounds. To further improve the performance of MOF-derived compound/BDD composites, it is necessary to enhance the specific surface area of BDD by synthesizing advanced diamond nanostructures, such as porous diamond, diamond fiber, and diamond foam, etc. These diamond nanostructures maintain the intrinsic properties of BDD while also providing a large surface area for energy storage and for loading pseudocapacitive materials. The development of flexible BDD is also desired to expand the application area of BDD electrode. This can be achieved by depositing BDD onto flexible substrates (e.g., carbon fibers). Moreover, despite the ongoing issue of high production costs for diamond, it surpasses other cost-effective electrodes in terms of longevity. Nonetheless, the primary challenge for future research on conductive diamond remains the development of

cost-efficient synthesis and processing methods to produce high-quality diamond in various forms. For industrial applications, the construction of ASC devices on a large scale and a further evaluation of their electrochemical performance are necessary.

Acknowledgement

S. Yu acknowledges the financial support from Fundamental Research Funds for the Central Universities of China (Grant No. SWU-KT22030) and Scientific and Technological Research Program of Chongqing Municipal Education Commission of China (No. KJQN202300205). N.Y. thanks the financial support from the Deutsche Forschungsgemeinschaft (DFG, German Research Foundation) under the project of 457444676.

Reference

[1] I. Shaheen, I. Hussain, T. Zahra, M.S. Javed, S.S.A. Shah, K. Khan, et al., Recent advancements in metal oxides for energy storage materials: Design, classification, and electrodes configuration of supercapacitor, J. Energy Storage 72 (2023) 108719.

[2] Y. Wang, L. Zhang, H. Hou, W. Xu, G. Duan, S. He, et al., Recent progress in carbon-based materials for supercapacitor electrodes: a review, J. Mater. Sci. 56 (2020) 173-200.

[3] N. Yang, S. Yu, W. Zhang, H.M. Cheng, P. Simon, X. Jiang, Electrochemical capacitors with confined redox electrolytes and porous electrodes, Adv. Mater. 34 (2022) 2202380.

[4] N. Yang, S. Yu, J.V. Macpherson, Y. Einaga, H. Zhao, G. Zhao, et al., Conductive diamond: synthesis, properties, and electrochemical applications, Chem. Soc. Rev. 48 (2019) 157-204.

[5] S. Yu, N. Yang, H. Zhuang, J. Meyer, S. Mandal, O.A. Williams, et al., Electrochemical supercapacitors from diamond, J. Phys. Chem. C 119 (2015) 18918-18926.

[6] S. Yu, N. Yang, S. Liu, X. Jiang, Diamond supercapacitors: progress and perspectives, Curr. Opin. Solid State Mater. Sci. 25 (2021) 100922.

[7] S. Deshmukh, S. Kunuku, P. Jakobczyk, A. Olejnik, C.H. Chen, H. Niu, et al., Diamond‐based supercapacitors with ultrahigh cyclic stability through dual‐phase MnO_2‐graphitic transformation induced by high‐dose Mn‐ion implantation, Adv. Funct. Mater. 34 (2023)

2308617.

[8] C. Shi, C. Li, M. Li, H. Li, W. Dai, Y. Wu, et al., Fabrication of porous boron-doped diamond electrodes by catalytic etching under hydrogen–argon plasma, Appl. Surf. Sci. 360, Part A (2016) 315-322.

[9] F. Gao, C.E. Nebel, Diamond nanowire forest decorated with nickel hydroxide as a pseudocapacitive material for fast charging–discharging, Phys. Status Solidi A 212 (2015) 2533-2538.

[10] C. Choi, D.S. Ashby, D.M. Butts, R.H. DeBlock, Q. Wei, J. Lau, et al., Achieving high energy density and high power density with pseudocapacitive materials, Nat. Rev. Mater. 5 (2020) 5-19.

[11] J. Huang, K. Yuan, Y. Chen, Wide voltage aqueous asymmetric supercapacitors: Advances, strategies, and challenges, Adv. Funct. Mater. 32 (2021).

[12] X. Wang, A. Hu, C. Meng, C. Wu, S. Yang, X. Hong, Recent advance in Co_3O_4 and Co_3O_4-containing electrode materials for high-performance supercapacitors, Molecules 25 (2020).

[13] S. Yang, L. Qian, Y. Ping, H. Zhang, J. Li, B. Xiong, et al., Electrochemical performance of Bi_2O_3 supercapacitors improved by surface vacancy defects, Ceram. Int. 47 (2021) 8290-8299.

[14] S. Wu, J. Liu, H. Wang, H. Yan, A review of performance optimization of MOF-derived metal oxide as electrode materials for supercapacitors, Int. J. Energy Res. 43 (2019) 697-716.

[15] M. Rad, S. Borhani, M. Moradi, V. Safarifard, Tuning the crystallinity of ZrO_2 nanostructures derived from thermolysis of Zr-based aspartic acid/succinic acid MOFs for energy storage application, Physica E 134 (2021) 114921.

[16] Y. Xiao, S. Li, C. Peng, N. Yang, S. Liu, S. Yu, Dual pseudocapacitive electrode/redox electrolyte systems for asymmetric supercabatteries, Appl. Surf. Sci. 616 (2023) 156552.

[17] S. Yu, N. Yang, M. Vogel, S. Mandal, O.A. Williams, S. Jiang, et al., Battery‐like supercapacitors from vertically aligned carbon nanofiber coated diamond: design and demonstrator, Adv. Energy Mater. 8 (2018) 1702947.

[18] W. Gajewski, P. Achatz, O.A. Williams, K. Haenen, E. Bustarret, M. Stutzmann, et al., Electronic and optical properties of boron-doped nanocrystalline diamond films, Phys. Rev. B

79 (2009) 045206.

[19] Y. Shao, M.F. El-Kady, J. Sun, Y. Li, Q. Zhang, M. Zhu, et al., Design and mechanisms of asymmetric supercapacitors, Chem. Rev. 118 (2018) 9233-9280.

[20] J. Lee, S. Choudhury, D. Weingarth, D. Kim, V. Presser, High performance hybrid energy storage with potassium ferricyanide redox electrolyte, ACS Appl. Mater. Interfaces 8 (2016) 23676-23687.

[21] J. Xu, N. Yang, S. Heuser, S. Yu, A. Schulte, H. Schönherr, et al., Achieving ultrahigh energy densities of supercapacitors with porous titanium carbide/boron-doped diamond composite electrodes, Adv. Energy Mater. 9 (2019) 1803623.

[22] C. Guan, W. Zhao, Y. Hu, Z. Lai, X. Li, S. Sun, et al., Cobalt oxide and N-doped carbon nanosheets derived from a single two-dimensional metal–organic framework precursor and their application in flexible asymmetric supercapacitors, Nanoscale Horiz. 2 (2017) 99-105.

[23] C. Liu, Q. Sun, L. Lin, J. Wang, C. Zhang, C. Xia, et al., Ternary MOF-on-MOF heterostructures with controllable architectural and compositional complexity via multiple selective assembly, Nature Commun. 11 (2020).

[24] X. Ma, Y.-X. Zhou, H. Liu, Y. Li, H.-L. Jiang, A MOF-derived Co–CoO@N-doped porous carbon for efficient tandem catalysis: dehydrogenation of ammonia borane and hydrogenation of nitro compounds, Chem. Commun. 52 (2016) 7719-7722.

[25] G. Jiang, N. Jiang, N. Zheng, X. Chen, J. Mao, G. Ding, et al., MOF-derived porous Co_3O_4-NC nanoflake arrays on carbon fiber cloth as stable hosts for dendrite-free Li metal anodes, Energy Storage Mater. 23 (2019) 181-189.

[26] X. Zhang, J. Wang, L. Xuan, Z. Zhu, Q. Pan, K. Shi, et al., Novel Co_3O_4 nanocrystalline chain material as a high performance gas sensor at room temperature, J. Alloys Compd. 768 (2018) 190-197.

[27] Y. Xu, Z. Liu, D. Chen, Y. Song, R. Wang, Synthesis and electrochemical properties of porous α-$Co(OH)_2$ and Co_3O_4 microspheres, Prog. Nat. Sci.: Mater. Int. 27 (2017) 197-202.

[28] H.S. Jadhav, A.K. Rai, J.Y. Lee, J. Kim, C.-J. Park, Enhanced electrochemical performance of flower-like Co_3O_4 as an anode material for high performance lithium-ion batteries, Electrochim. Acta 146 (2014) 270-277.

[29] X. Wang, F. Wang, L. Wang, M. Li, Y. Wang, B. Chen, et al., An aqueous rechargeable

Zn//Co_3O_4 battery with high energy density and good cycling behavior, Adv. Mater. 28 (2016) 4904-4911.

[30] Y. Tan, Q. Gao, C. Yang, K. Yang, W. Tian, L. Zhu, One-dimensional porous nanofibers of Co_3O_4 on the carbon matrix from human hair with superior lithium ion storage performance, Sci. Rep. 5 (2015) 12382.

[31] H. Zhang, B. Yan, C. Zhou, J. Wang, H. Duan, D. Zhang, et al., MOF-derived hollow and porous Co_3O_4 nanocages for superior hybrid supercapacitor electrodes, Energy Fuels 35 (2021) 16925-16932.

[32] S. Li, K. Yang, P. Ye, K. Ma, Z. Zhang, Q. Huang, Three-dimensional porous carbon/Co_3O_4 composites derived from graphene/Co-MOF for high performance supercapacitor electrodes, Appl. Surface Sci. 503 (2020) 144090.

[33] Y.-W. Cheng, R.K. Pandey, Y.-C. Li, C.-H. Chen, B.-L. Peng, J.-H. Huang, et al., Conducting nitrogen-incorporated ultrananocrystalline diamond coating for highly structural stable anode materials in lithium ion battery, Nano Energy 74 (2020) 104811.

[34] Y. Dou, T. Liao, Z. Ma, D. Tian, Q. Liu, F. Xiao, et al., Graphene-like holey Co_3O_4 nanosheets as a highly efficient catalyst for oxygen evolution reaction, Nano Energy 30 (2016) 267-275.

[35] V.G. Hadjiev, M.N. Iliev, I.V. Vergilov, The Raman spectra of Co_3O_4, J. Phys. C: Solid State Phys. 21 (1988) L199-L201.

[36] L.X. Dien, H.D. Chinh, N.K. Nga, R. Luque, S.M. Osman, L.G. Voskressensky, et al., Facile synthesis of Co_3O_4@SiO_2/carbon nanocomposite catalysts from rice husk for low-temperature CO oxidation, Mol. Catal. 518 (2022) 112053.

[37] F. Gao, M.T. Wolfer, C.E. Nebel, Highly porous diamond foam as a thin-film micro-supercapacitor material, Carbon 80 (2014) 833-840.

[38] X. Yu, J. Sun, W. Zhao, S. Zhao, H. Chen, K. Tao, et al., MOF-derived Bi_2O_3@C microrods as negative electrodes for advanced asymmetric supercapacitors, RSC Adv. 10 (2020) 14107-14112.

[39] A.K. Inge, M. Koppen, J. Su, M. Feyand, H. Xu, X. Zou, et al., Unprecedented topological complexity in a metal-organic framework constructed from simple building units, J. Am. Chem. Soc. 138 (2016) 1970-6.

[40] X. Li, C. Guan, Y. Hu, J. Wang, Nanoflakes of Ni-Co LDH and Bi_2O_3 assembled in 3D carbon fiber network for high-performance aqueous rechargeable Ni/Bi battery, ACS Appl. Mater. Interfaces 9 (2017) 26008-26015.

[41] P. Zhang, Y. Wei, S. Zhou, R.A. Soomro, M. Jiang, B. Xu, A metal-organic framework derived approach to fabricate in-situ carbon encapsulated Bi/Bi_2O_3 heterostructures as high-performance anodes for potassium ion batteries, J. Colloid Interface Sci. 630 (2023) 365-374.

[42] Z. Ji, W. Dai, S. Zhang, G. Wang, X. Shen, K. Liu, et al., Bismuth oxide/nitrogen-doped carbon dots hollow and porous hierarchitectures for high-performance asymmetric supercapacitors, Adv. Powder Technol. 31 (2020) 632-638.

[43] J. Zhao, Z. Li, T. Shen, X. Yuan, G. Qiu, Q. Jiang, et al., Oxygen-vacancy Bi_2O_3 nanosheet arrays with excellent rate capability and $CoNi_2S_4$ nanoparticles immobilized on N-doped graphene nanotubes as robust electrode materials for high-energy asymmetric supercapacitors, J. Mater. Chem. A 7 (2019) 7918-7931.

[44] C. Wang, Q. Niu, D. Liu, X. Dong, T. You, Electrochemical sensor based on Bi/Bi_2O_3 doped porous carbon composite derived from Bi-MOFs for Pb^{2+} sensitive detection, Talanta 258 (2023) 124281.

[45] X. Li, W. Zhang, M. Wu, S. Li, X. Li, Z. Li, Multiple-heteroatom doped porous carbons from self-activation of lignosulfonate with melamine for high performance supercapacitors, Int. J. Biol. Macromol. 183 (2021) 950-961.

[46] I.M. Babu, J.J. William, G. Muralidharan, Ordered mesoporous Co_3O_4/CMC nanoflakes for superior cyclic life and ultra high energy density supercapacitor, Appl. Surf. Sci. 480 (2019) 371-383.

[47] Q. Liu, Q. Zhou, C. Gao, L. Liu, H. Ye, Excellent electrochemical stability of Co_3O_4 array with carbon hybridization derived from metal-organic framework, Nanotechnol. 32 (2021) 485710.

[48] R. Khayyam Nekouei, S. S. Mofarah, S. Maroufi, I. Tudela, V. Sahajwalla, Determination of the optimum potential window for super- and pseudocapacitance electrodes via in-depth electrochemical impedance spectroscopy analysis, J. Energy Storage 56 (2022) 106137.

[49] C.G. Real, R. Vicentini, W.G. Nunes, A.M. Pascon, F.A. Campos, L.M. Da Silva, et al.,

Analyses of dispersive effects and the distributed capacitance in the time and frequency domains of activated carbon nanofiber electrodes as symmetric supercapacitors, Electrochim. Acta 402 (2022) 139299.

[50] Y. Ma, Y. Bai, B. Liang, R. Yang, S. Zheng, C. Hu, et al., MOF-derived hierarchical Bi_2O_3 as advanced anode for Ni/Bi alkaline battery with high energy density, Colloids Surf., A 633 (2022) 127896.

[51] S.M. Mbam, R.M. Obodo, O.O. Apeh, A.C. Nwanya, A.B.C. Ekwealor, N. Nwulu, et al., Performance evaluation of Bi_2O_3@GO and Bi_2O_3@rGO composites electrode for supercapacitor application, J. Mater. Sci.: Mater. Electron. 34 (2023) 1405.

[52] Y. Wang, J. Zhou, K. Chen, W. Zhao, K. Tao, L. Han, Metal–organic framework-derived Bi_2O_3/C and $NiCo_2S_4$ hollow nanofibers for asymmetric supercapacitors, ACS Appl. Nano Mater. 4 (2021) 11895-11906.

[53] H. Zheng, H. Li, M. Yu, M. Zhang, Y. Tong, F. Cheng, et al., Vertical bismuth oxide nanosheets with enhanced crystallinity: promising stable anodes for rechargeable alkaline batteries, J. Mater. Chem. A 5 (2017) 25539-25544.

[54] H. Mei, H. Zhang, Y. Bai, K. Zhang, Z. Li, J. Gao, et al., Enabling the fabrication of advanced NiCo/Bi alkaline battery via MOF-hydrolyzing derived cathode and anode, Mater. Today Phys. 21 (2021) 100499.

[55] S. Deshmukh, P. Jakobczyk, M. Ficek, J. Ryl, D. Geng, R. Bogdanowicz, Tuning the laser‐induced processing of 3D porous graphenic nanostructures by boron‐doped diamond particles for flexible microsupercapacitors, Adv. Funct. Mater. 32 (2022).

[56] E. Scorsone, N. Gattout, L. Rousseau, G. Lissorgues, Porous diamond pouch cell supercapacitors, Diamond Relat. Mater. 76 (2017) 31-37.